Journal of Alloys and Compounds 1037 (2025) 182542

Contents lists available at ScienceDirect

Journal of Alloys and Compounds

journal homepage: www.elsevier.com/locate/jalcom

Enhanced NH_3 sensing performance of $Ti_3C_2T_x$ MXene decorated with flowered MoS_2

Lizhai Zhang [a,b,c,*], Xinyu Lei [a], Henghui Sun [a], Dingyuan Wang [a], Baisong Chen [d], Fei Ma [b], Taotao Ai [a,**], Paul K. Chu [c,**]

[a] School of Materials Science and Engineering, Shaanxi University of Technology, Hanzhong, Shaanxi 723001, China
[b] State Key Laboratory for Mechanical Behavior of Materials, Xi'an Jiaotong University, Xi'an, Shaanxi 710049, China
[c] Department of Physics, Department of Materials Science and Engineering, and Department of Biomedical Engineering, City University of Hong Kong, Tat Chee Avenue, Kowloon, Hong Kong
[d] Faculty of Optoelectronic Engineering, Xidian University, Xi'an, Shaanxi 710126, China

ARTICLE INFO

Keywords:
$MoS_2/Ti_3C_2T_x$ MXene
Heterojunction
NH_3 sensor
Nanocomposites

ABSTRACT

Because of abundant terminal groups, metal electrical conductivity and multilayer structure, the $Ti_3C_2T_x$ have attracted extensive application for detection of harmful gas. However, the poor reversibility and response limit its application. Herein, the edge-enriched MoS_2 and $Ti_3C_2T_x$ heterostructure was prepared hydrothermally and applied for NH_3 detection. The growth of flower-like MoS_2 on multilayer structure of $Ti_3C_2T_x$ could increase number of edge sites for NH_3 adsorption. This synergistic effect has led into a 553 % and 3060 % improvement in sensing response compared to pure MoS_2 and $Ti_3C_2T_x$ on exposure to 300 ppm of NH_3 at RT.The DFT calculations reveal that the heterojunction could improve the activity of charge transfer between the sensor and NH_3 molecular, enhancing the NH_3-sensing response. These findings offer the valuable insights for the room-temperature NH_3 detection.

1. Introduction

Air pollution is becoming more serious due to the emission of NO_2, CO, CO_2, and NH_3 from industrial production, fossil fuel combustion, and automobile exhaust [1–5]. Among them, NH_3, a colorless gas with a strong odor, can cause irritation to the eye, skin, and throat, and even health hazards [6–9]. Additionally, the NH_3 molecular could serve as a biomarker for kidney and liver disorders, which enables the early detection of cancer [6–9]. Therefore, it is necessary to develop a simple, portable, and stable sensor to detect NH_3 quickly and reliably.

Because of large specific surface area, high electrical conductivity, and abundant functional groups (-F, -OH, etc.), $Ti_3C_2T_x$ has been investigated as an NH_3-sensing material theoretically and experimentally. For example, Tan et al. have prepared layered $Ti_3C_2T_x$ by etching Ti_3AlC_2 with HF, and the response to 200 ppm NH_3 is about 7.6 % at room temperature (RT). The response and recovery time are about 83 s and 84 s, respectively [10]. Khakbaz et al. have calculated the adsorption energies of $Ti_3C_2T_x$ toward NH_3 and other gas molecules (NO, NO_2, N_2O, CO, CO_2, CH_4, and H_2S) by the first-principles calculations, and found that of $Ti_3C_2T_x$ toward NH_3 is much more negative than that of other gas, resulting in the higher NH_3 sensing response [11]. Wu et al. have prepared single-layer $Ti_3C_2T_x$ dispersion by intercalation and ultrasonic, and the response to 500 ppm NH_3 is about 6.13 % at RT [12]. Nevertheless, due to the strong interlayer van der Waals forces, the self-stacking of $Ti_3C_2T_x$ occurs easily, resulting in the poor sensing response (below 10 %) at RT. In addition, the $Ti_3C_2T_x$ is easily oxidized in air, behaving the poor reversibility.

To address these challenges, the NH_3-sensing performance of $Ti_3C_2T_x$ can be enhanced by combining with other materials. For example, Guo et al. have synthesized $Ti_3C_2T_x$ and WO_3 composites ultrasonically. Compared with $Ti_3C_2T_x$, the response of composites toward 1 ppm NH_3 at RT increases by 15.4 times [13]. Zhou et al. have synthesized $Ti_3C_2T_x$ and In_2O_3 nanocomposites ultrasonically and found the response to 30 ppm NH_3 at RT is about 63.8 %, which is 30.4 times higher than that of $Ti_3C_2T_x$ [14]. Lee et al. have prepared $Ti_3C_2T_x$ and graphene fibers by scalable wet spinning with enhanced NH_3 sensing response compared to individual $Ti_3C_2T_x$ and graphene [15]. MoS_2 is a semiconducting two-dimensional (2D) transition metal dichalcogenide (TMD) boasting

* Corresponding author at: School of Materials Science and Engineering, Shaanxi University of Technology, Hanzhong, Shaanxi 723001, China.
** Corresponding authors.
E-mail addresses: zhanglizhai0512@snut.edu.cn (L. Zhang), aitaotao0116@126.com (T. Ai), paul.chu@cityu.edu.hk (P.K. Chu).

https://doi.org/10.1016/j.jallcom.2025.182542
Received 17 March 2025; Received in revised form 5 July 2025; Accepted 24 July 2025
Available online 24 July 2025

Fig. 1. Flow chart of the experiment.

high carrier mobility, large adsorption coefficient, and tunable band gaps. It may have a positive impact on the sensitivity and stability of gas sensors if the MoS_2 is composited with $Ti_3C_2T_x$.

Herein, the composites of MoS_2 and $Ti_3C_2T_x$ MXene are synthesized hydrothermally. The growth of MoS_2 on the surface of $Ti_3C_2T_x$ could prevent restacking and oxidation of $Ti_3C_2T_x$. And the large surface area of conducting $Ti_3C_2T_x$ acts as a template for MoS_2, generating more interfacial sites for NH_3 molecular adsorption. Compared with pure MoS_2 and $Ti_3C_2T_x$, the response of composites toward 300 ppm NH_3 at RT is obviously enhanced. In addition, the first-principles calculation was used to reveal the mechanism of enhanced gas sensing performance.

2. Experimental details

2.1. Preparation of MoS_2 and $Ti_3C_2T_x$ composites

As displayed in Fig. 1, the MoS_2 and $Ti_3C_2T_x$ MXene composites were prepared by a hydrothermal method. Firstly, $Ti_3C_2T_x$ MXene (10 mg) was dissolved in 30 mL of distilled water and stirred for 30 min, followed by addition of 0.35 g of sodium molybdate ($Na_2MoO_4{\cdot}2\,H_2O$) and 0.25 g (0.7 wt%), 0.3 g (0.85 wt%), 0.35 g (1.0 wt%), 0.4 g (1.15 wt%), or 0.45 g (1.3 wt%) of thiourea (relative to 0.35 g of $Na_2MoO_4{\cdot}2\,H_2O$), respectively, and subsequent stirring for 1 h. The mixture was transferred to a 50 mL polytetrafluoroethylene reactor and reacted hydrothermally at 200 ℃ for 24 h. After cooling to room temperature, the black product was collected, filtered, centrifuged, washed with anhydrous ethanol and distilled water three times repeatedly, and then placed in a vacuum oven at 60 ℃ for 10 h to prevent oxidization, and finally milled to obtain the five samples of composites, which was designated as $MoS_2/Ti_3C_2T_x$-a, $MoS_2/Ti_3C_2T_x$-b, $MoS_2/Ti_3C_2T_x$-c, $MoS_2/Ti_3C_2T_x$-d and $MoS_2/Ti_3C_2T_x$-e, respectively.

2.2. Characterization and testing

X-ray diffraction (XRD, D/max-2200PC) with Cu-Kα radiation (40 kV, 30 mA) was used to characterize the phase composition and scanning angle (2θ) was ranged from 5° to 90°. The scanning electron microscope (SEM, JSM-7610F) and transmission electron microscope (TEM, JEM-2100P, 200 Kv) were performed to examine the microstructure and morphology. Energy-dispersive X-ray spectrometry (EDS, JSM-7610F) was used to determine the elemental composition and distribution. X-ray photoelectron spectroscopy (XPS, Thermo Scientific K-Alpha) was conducted to determine the chemical states. During the spectral acquisition process, the vacuum degree of the analysis chamber is approximately 5×10^{-9} mbar. The X-ray source energy is 1486.6 eV. The operating voltage is set at 12 eV, the beam current is 6 mA, the analyzer scanning mode is CAE. The full-spectrum energy is 150 eV, with a step size of 1 eV. The fine-spectrum energy is 50 eV, and the step size is 0.1 eV. The instrument work function is 4.2 eV. The analysis region is a circle with a diameter of 400 μm. During the experiment, a 10 mg powder sample was directly adhered using double-sided carbon conductive adhesive or ordinary double-sided adhesive and loaded into

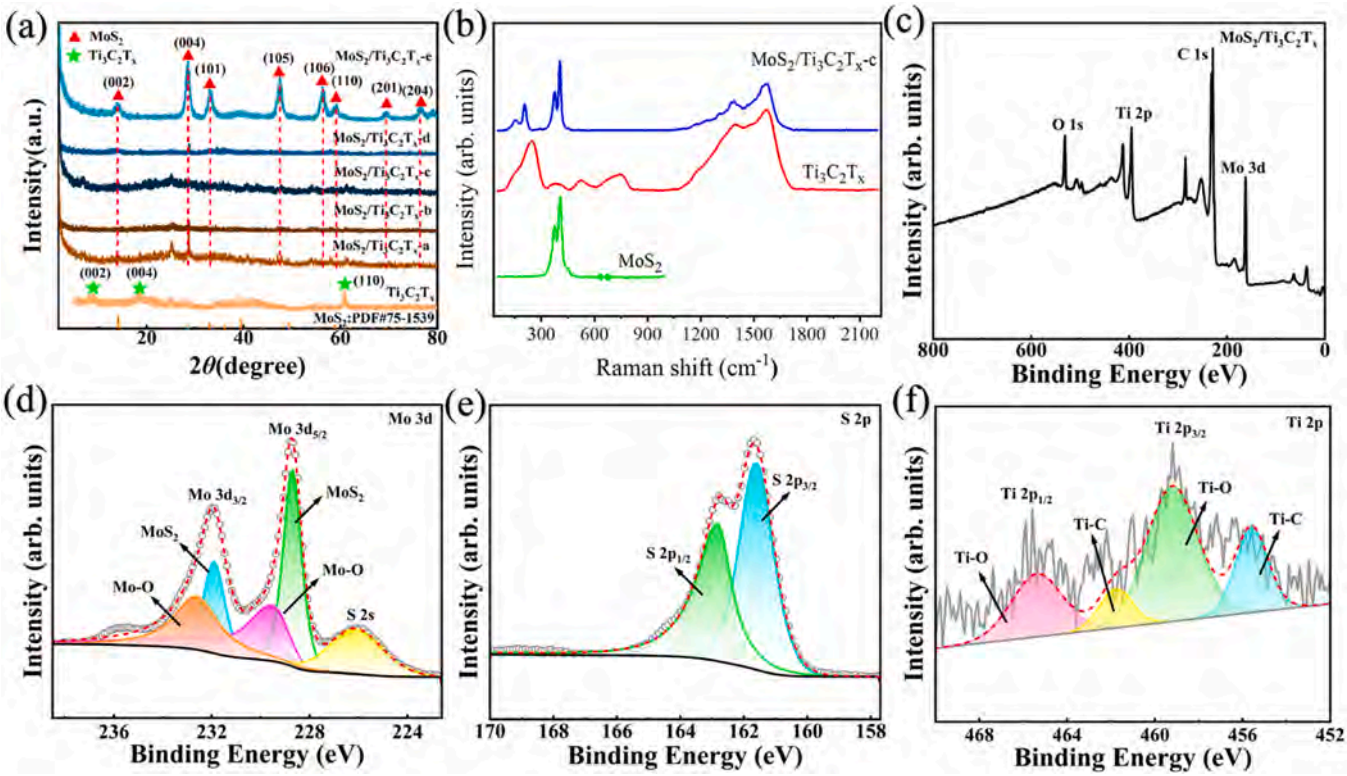

Fig. 2. Structural characterization of the $MoS_2/Ti_3C_2T_x$ MXene composites: (a) XRD patterns of $Ti_3C_2T_x$ MXene [9] and composites; (b) Raman scattering spectrum of MoS_2 and $MoS_2/Ti_3C_2T_x$-c; (c-f) XPS spectra of $MoS_2/Ti_3C_2T_x$-c.

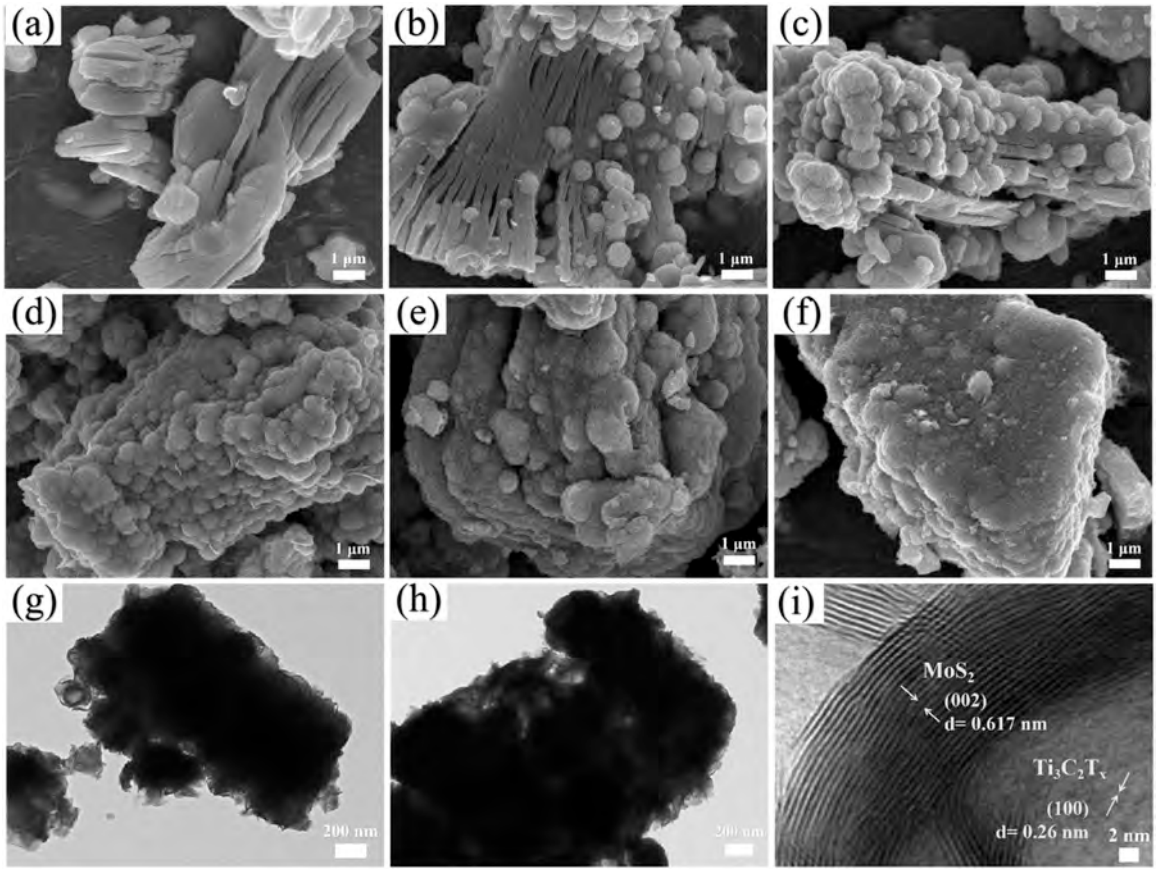

Fig. 3. The SEM image of (a) $Ti_3C_2T_x$ and $MoS_2/Ti_3C_2T_x$ composites prepared with (b) 0.7 wt%, (c) 0.85 wt%, (d) 1.0 wt%, (e) 1.15 wt%, and (f) 1.3 wt% thiourea concentration; (g, h) TEM and (i) HR-TEM images of $MoS_2/Ti_3C_2T_x$-c.

the spectrometer for testing. Raman scattering (Horiba LabRAM HR Evolution, 514 nm) was used to study the vibrational states.

2.3. Fabrication of gas sensors and measurement

The 5 mg of samples were added into 1 mL distilled water to form a slurry, uniformly coated on a gold-forked finger electrode with a width of 5 mm, and dried at RT (296.15 K) for 24 h. The sensing properties were determined on a CGS-8 intelligent gas-sensitive analyzer system (Beijing Zhongju Hi-Tech Co., Ltd., China) at 296.15 K. Ammonia (NH_3) gas was obtained by evaporating aqueous ammonia solution (25 *wt*%). The concentration of NH_3 was calculated according to the Eq. 1:

$$\mathbb{C} = (22.4 \times \rho \times \mathscr{A} \times \mathscr{V}_1)/(M \times \mathscr{V}_2) \quad (1)$$

where, $\mathbb{C}$ is the concentration of gas (ppm), the density of the liquid is indicated by ρ (g/mL), The purity of organic liquid is denoted by $\mathscr{A}$, $\mathscr{V}_1$ (μL) and $\mathscr{V}_2$ (L) represent the volume of the organic liquid and the cavity, respectively. M (g/mol) is the molar mass of organic matter. Environmental humidity is controlled by filling the evaporator with an aqueous solution. The sensing response (S) is defined as:

$$S = \left|\frac{R_g - R_a}{R_a}\right| \times 100\% \quad (2)$$

where R_g is the resistance of sensor for target gas, and R_a is the resistance of sensor in air. The response time is defined as the time required for the signal to rise from zero to 90 % of the maximum response, and the recovery time is the time required for the resistance of sensor to recover to 10 % of the initial resistance.

2.4. DFT calculation

The density states of MoS_2, $Ti_3C_2T_x$, and $MoS_2/Ti_3C_2T_x$ heterojunction were determined by density-functional theory simulation based on Vienna ab initio calculations [16–18]. The Perdew-Burke-Ernzerhof (PBE) was used as the exchange-correlation function. The kinetic energy cutoff and force threshold were 500 eV and 0.05 eV/Å, respectively. The Monkhorst-pack k-point grids were set as 3 × 3 × 1 and 5 × 5 × 1 to optimize the structure and energy, respectively. The vacuum slab was 10 Å in the z-direction. The adsorption energy (E_{ads}) of sensor toward gas molecular is calculated by Eq. (3):

$$E_{ads} = E_{Sensor+gas} - E_{Sensor} - E_{gas} \quad (3)$$

where$E_{Sensor+NH_3}$, E_{Sensor}, and E_{NH_3} are the total energy of sensor with adsorbed gas molecular, pure sensor and gas molecule, respectively. The more negative behaves the stronger adsorption ability.

3. Results and discussion

3.1. Structure characterization

The XRD is conducted to determine the crystal structure of $Ti_3C_2T_x$ and $MoS_2/Ti_3C_2T_x$ composites. As illustrated in Fig. 2a, the diffraction peaks at about 8.12°, 18.54° and 60.89° are arise from the (002), (004) and (110) crystal plane of $Ti_3C_2T_x$ [9]. For the $MoS_2/Ti_3C_2T_x$ composites, the diffraction peaks at about 13.86°, 28.57°, 33.12°, 47.55°, 56.35°, 59.10°, 69.69° and 76.71° are arise from the (002), (004), (101), (105), (106), (110), (201) and (204) crystal planes of MoS_2, which can be indexed to the 2 H structure of MoS_2 (JCPDS: PDF#75–1539). The diffraction peaks of $Ti_3C_2T_x$ in composites couldn't be observed, which

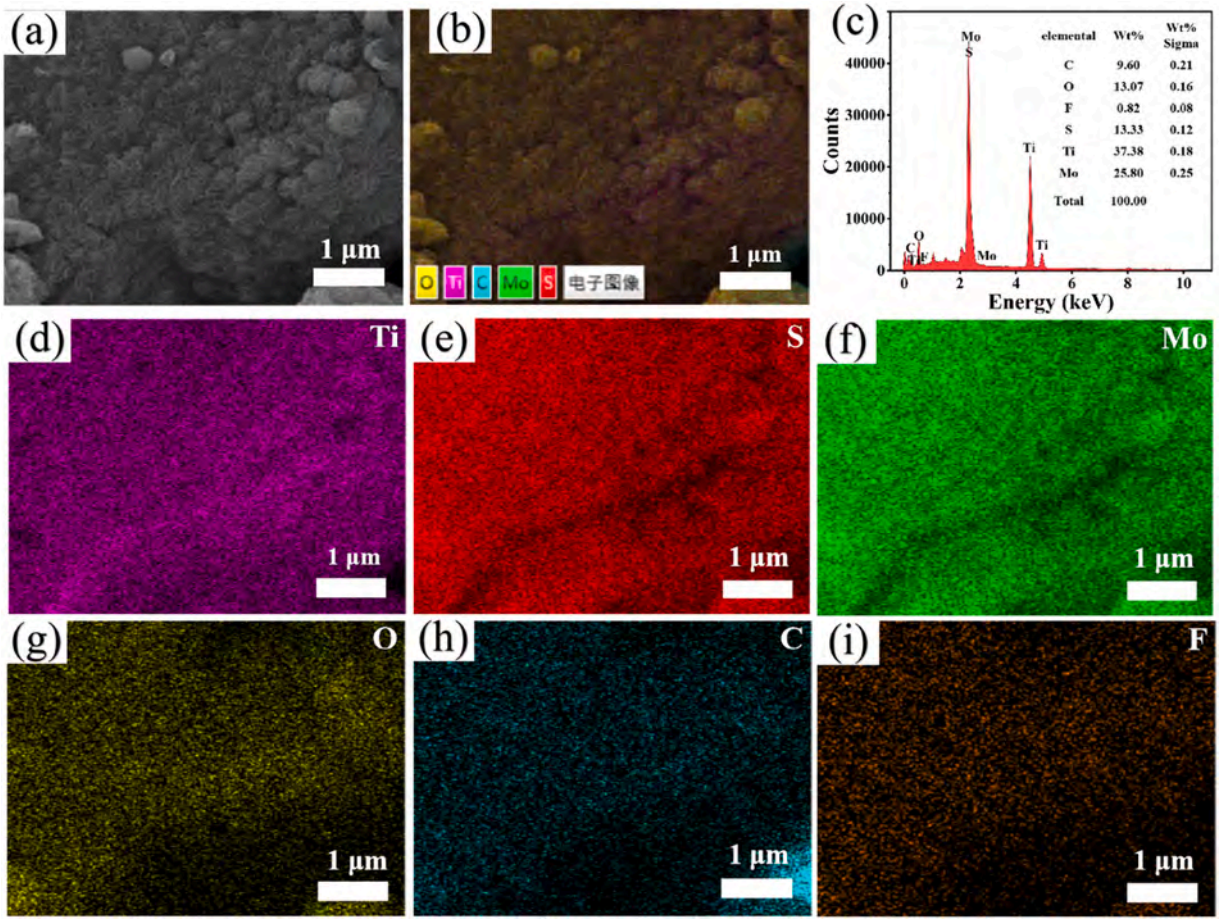

Fig. 4. EDS patterns of $MoS_2/Ti_3C_2T_x$-c: (a, b) SEM image; (b) Spectrum; (d-i) Elemental maps of Ti, S, Mo, O, C, and F.

due to the surface of $Ti_3C_2T_x$ is encapsulated by MoS_2. The intensity of XRD peak of MoS_2 in composites is enhanced with increase of thiourea concentration. During preparation, the thiourea is served as the reducing agent and sulfur source. At low thiourea concentration, a small amount of Na_2MoO_4 could react with thiourea, resulting in poor crystallinity of MoS_2. Hence, the diffraction peaks of MoS_2 are poor. With increase of thiourea concentration, the lots of Na_2MoO_4 could react with thiourea, and a great amount of MoS_2 are formed on the surface of $Ti_3C_2T_x$. Hence, the XRD peak of MoS_2 in composites is clearly observed. The Raman spectra of MoS_2, $Ti_3C_2T_x$ and composites are displayed in Fig. 2b. The Raman peaks at about 384.2 cm^{-1} (in-plane $E^1_{2\,g}$ mode) and 406.8 cm^{-1} (out-of-plane $A_{1\,g}$ mode) corresponds to the MoS_2 [19]. The Raman peaks at about 248.36 cm^{-1}, 1354.93 cm^{-1} and 1592.4 cm^{-1} arises from the $Ti_3C_2T_x$. As for the composites, the Raman peaks of MoS_2 and $Ti_3C_2T_x$ are occurred in the composites, indicating that MoS_2 hybridizes with $Ti_3C_2T_x$ MXene to form the composites.

The pure MoS_2 and $Ti_3C_2T_x$ were characterized by XPS and the results were shown in Fig. S1. In Fig. S1a, the peaks at about 228.9 eV and 232.1 eV are corresponded to the Mo $3d_{5/2}$ and Mo $3d_{3/2}$, respectively, confirming formation of 2H-MoS_2. In Fig. S1b, the peaks at about 161.9 eV and 163.2 eV are attributed to the S 2p3/2 and S 2p1/2. The measured spectrum of $Ti_3C_2T_x$ were displayed in Fig. S1c and S1d. In Fig. S1c, the Ti 2p spectra of $Ti_3C_2T_x$ could be fitted into four peaks at about 454.3 eV, 458.9 eV, 461.3 eV and 465.1 eV, which are attributed to the Ti-$C_{3/2}$, Ti $2p_{3/2}$ (Ti-$O_{3/2}$), Ti-$C_{1/2}$, and Ti $2p_{1/2}$ (Ti-$O_{1/2}$), respectively. During the hydrothermal process, part of $Ti_3C_2T_x$ was oxidized to TiO_2, forming the Ti-O bonds. As displayed in Fig. S1d, the C1s spectrum could be divided into three peaks with binding energies of 281.3 eV, 285 eV, and 287.5 eV, which corresponding to the Ti-C, C-C, and C-O valence states, respectively. The survey spectrum of MoS_2 and $Ti_3C_2T_x$ composites were measured and the results were displayed in Fig. 2c. The C, Ti, Mo and S peaks are clearly observed in the survey spectrum. In Fig. 2(d-f), the binding energies of Mo 3d (Mo 3d5/2 and Mo 3d3/2) and S 2p (S 2p3/2 and S 2p1/2) spectra are decreased to 228.74 eV, 231.99 eV, 161.65 eV and 162.76 eV, respectively. While, the binding energy of Ti 2*p* spectra (Ti-$C_{3/2}$, Ti $2p_{3/2}$ (Ti-$O_{3/2}$), Ti-$C_{1/2}$, and Ti $2p_{1/2}$ (Ti-$O_{1/2}$)) are increased to 455.58 eV, 459.19 eV, 461.78 eV, and 465.38 eV, respectively. The results confirm the electron exchange occurs at interface of MoS_2 and $Ti_3C_2T_x$.

The microstructures of $Ti_3C_2T_x$ and $MoS_2/Ti_3C_2T_x$ composites were measured by SEM. As shown in Fig. 3a, $Ti_3C_2T_x$ MXene behaves the typical multilayered lamellar structure. The microstructure of MoS_2 in the composites depends on the content of thiourea during preparation. When the concentration of thiourea is 0.7 wt%, the sparse-flower globular MoS_2 is grown on the surface of $Ti_3C_2T_x$. If the thiourea concentration is added up from 0.70 wt% to 1.0 wt%, the density of MoS_2 is increased and uniformly cover $Ti_3C_2T_x$ MXene (Fig. 3b-d). If the thiourea concentration is increased further, the MoS_2 morphs gradually into flower-like nanosheets (Fig. 3e and f). Fig. 3g and h display the TEM images of $MoS_2/Ti_3C_2T_x$ composites (1.0 wt%), revealing that the flower-like MoS_2 are grown on the surface of MXene and behaving the layered structure. The layer spacings of 0.617 nm and 0.26 nm are attributed to the (002) plane of MoS_2 and (100) plane of $Ti_3C_2T_x$, respectively (Fig. 3i). The EDS mapping of the $MoS_2/Ti_3C_2T_x$ composite (1.0 wt%) is also conducted. As displayed in Fig. 4, the S and Mo element are uniformly distributed on the $Ti_3C_2T_x$, which further reveals the growth of MoS_2 on the surface of $Ti_3C_2T_x$.

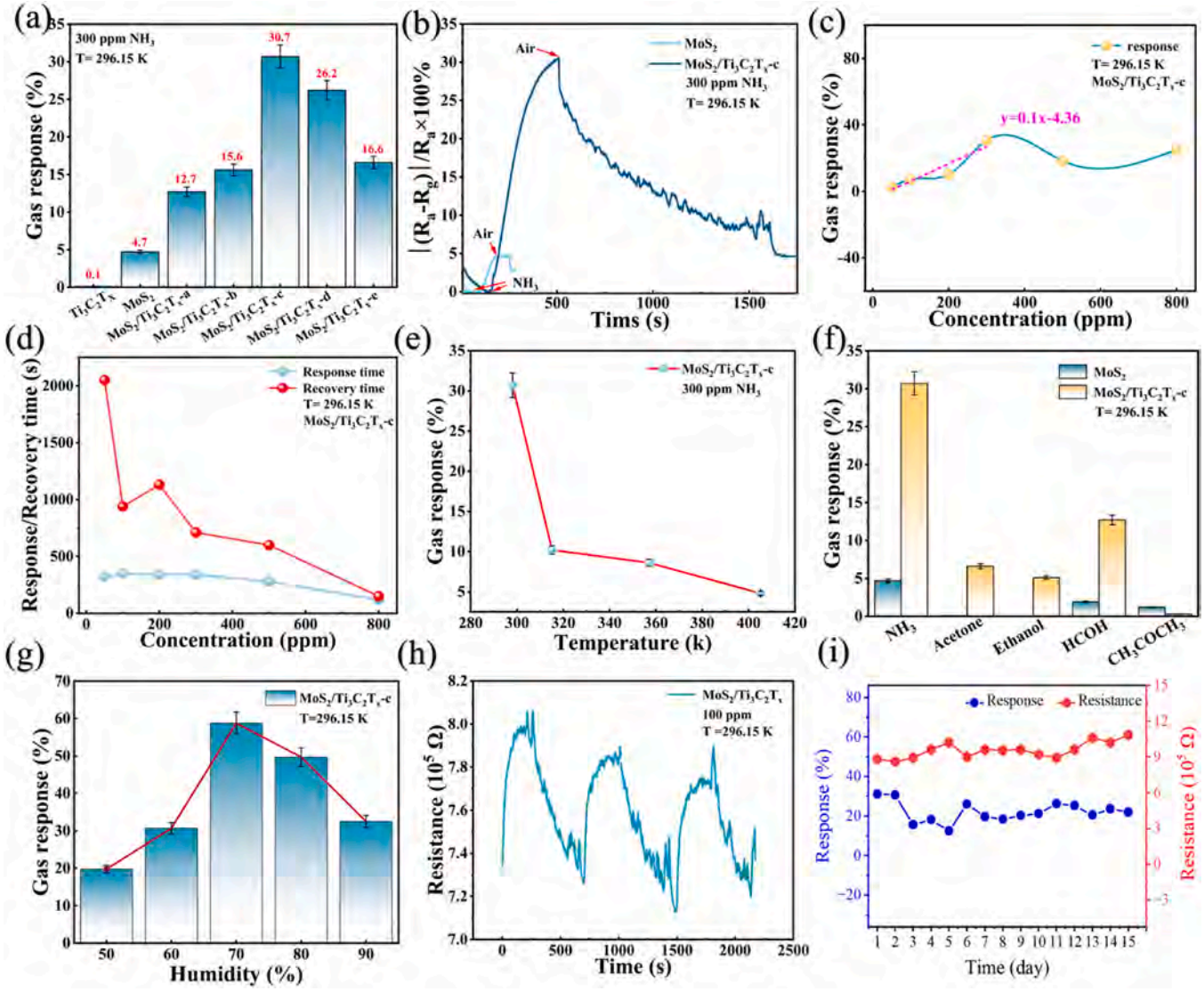

Fig. 5. (a) Response of MoS_2, $Ti_3C_2T_x$ and composites to 300 ppm NH_3 at RT; (b) Dynamic response-recovery curves of MoS_2 and $MoS_2/Ti_3C_2T_x$-c to 300 ppm NH_3 at RT; (c) Response of $MoS_2/Ti_3C_2T_x$-c sensor to different NH_3 concentrations at RT; (d) Response/recovery time of $MoS_2/Ti_3C_2T_x$-c to different NH_3 concentrations at RT; (e) Response of $MoS_2/Ti_3C_2T_x$-c to 300 ppm NH_3 at different temperatures; (f) Response of MoS_2 and $MoS_2/Ti_3C_2T_x$-c to different gases; (g) Response of $MoS_2/Ti_3C_2T_x$-c to 300 ppm NH_3 at different humidity; (h) Cycling response performance of $MoS_2/Ti_3C_2T_x$-c; (i) Stability of $MoS_2/Ti_3C_2T_x$ MXene-c.

3.2. Gas sensing properties

The room-temperature NH_3-sensing performance of MoS_2, $Ti_3C_2T_x$, and composites is investigated. As illustrated in Fig. 5**a**, the response of MoS_2 and $Ti_3C_2T_x$ is only 4.7 % and 0.1 %, which is much smaller than that of composites. In addition, if the content of thiourea is increased from 0.7 to 1.0 *wt*%, the response of composites is enhanced, but upon further increase, the response becomes poorer. According to SEM, if the concentration of thiourea is 1.0 wt% during preparation, the MoS_2 exhibits the flower globular structure and is uniformly grown on the surface of $Ti_3C_2T_x$, resulting in a larger specific surface area and better NH_3 adsorption. Thus, the composites of MoS_2 and $Ti_3C_2T_x$ prepared at 1.0 wt% thiourea ($MoS_2/Ti_3C_2T_x$-c) shows the highest response to NH_3 at RT and is further studied. Fig. 5**b** shows the response change curves of MoS_2 and $MoS_2/Ti_3C_2T_x$-c to 300 ppm NH_3 at RT. Compared to pure MoS_2, the response of composites is enhanced by 650 % as well as the response and recovery time are reduced to 340 s and 710 s, respectively. Fig. 5**c** shows the response of $MoS_2/Ti_3C_2T_x$-c sensor toward different NH_3 concentrations (50–800 ppm) at RT. As the NH_3 concentration is increased from 50 ppm to 300 ppm, the response is obviously enhanced and shows a better linear relationship ($R^2 = 0.875$). The response is enhanced by 0.1 % when the NH_3 concentration is increased by 1 ppm. If the NH_3 concentration is further increased, the response reaches saturation. At low NH_3 concentrations, the most sites are available and the charge transfer is proportional to the gas concentration. While, at higher NH_3 concentrations, all the active sites may be occupied, and the response reaches saturation [20–23]. The lowest detection limit (*LDL*) is calculated by Eq. (4)[22]:

$$LDL = 3 \times \frac{RMS}{Slope} \tag{4}$$

where *RMS* represents the root-mean-square of noise, and the slope is calculated from the linear response [22]. The *LDL* of $MoS_2/Ti_3C_2T_x$-c sensor is calculated to be about 1.986 ppm. In addition, the response and recovery time decrease with increasing NH_3 concentration (Fig. 5d). Fig. 5**e** shows the response of $MoS_2/Ti_3C_2T_x$-c composite to 300 ppm NH_3 at different temperatures. The response decreases with increase of temperature due to reduced NH_3 adsorption at active site and enhanced desorption [20]. Moreover, the MoS_2 substrate may be oxidized during heating, resulting in a poor response at higher temperatures [24].

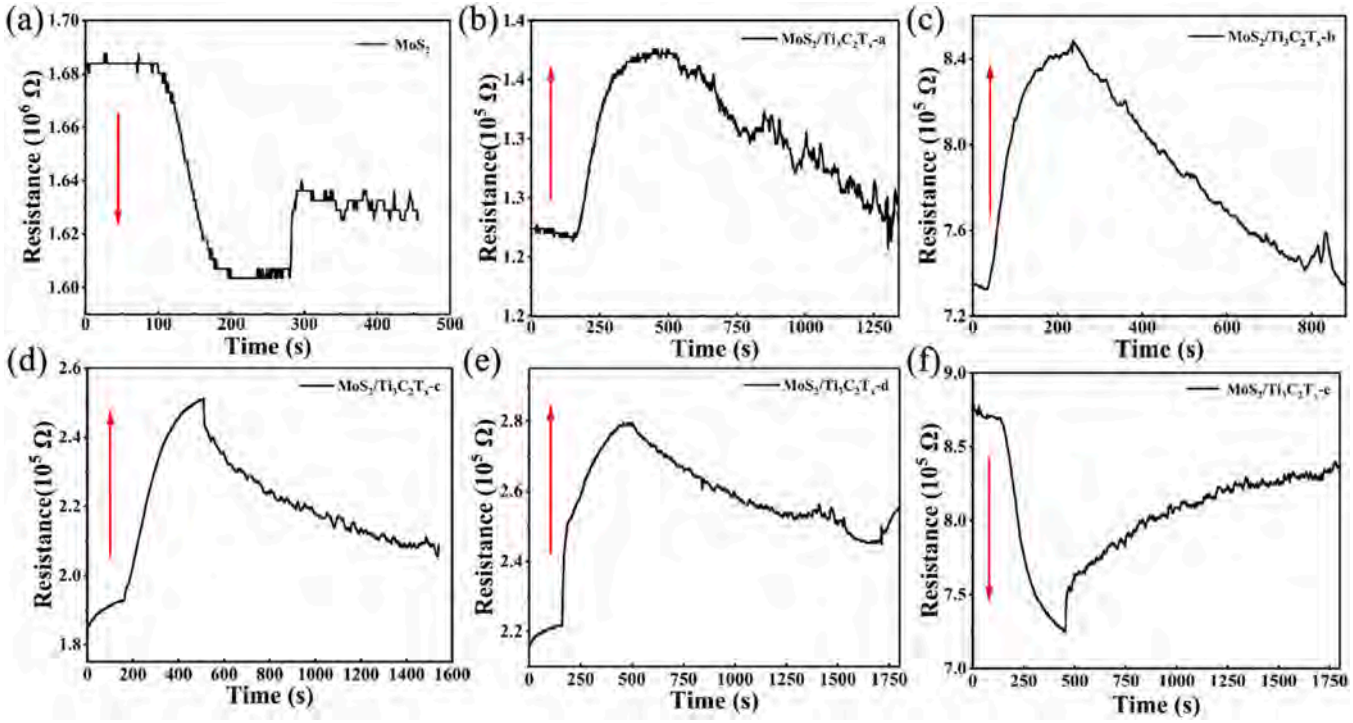

Fig. 6. Resistance change curves of (a) MoS_2 and (b-f) $MoS_2/Ti_3C_2T_x$ composites a-e in NH_3 at RT.

Therefore, RT is the optimal operating temperature. In Fig. 5**f**, the response of MoS_2 and $Ti_3C_2T_x$ composites toward 300 ppm NH_3 at RT is much higher than that of acetone, ethanol, HCOH and CH_3COCH_3, behaving the excellent selectivity performance [20,25–27]. According to the knudsen diffusion theory, the diffusion rate of gases can be correlated to their molecular weight. The higher molecular weight means the poorer diffusion rate. In addition, to reveal the selectivity trends of MoS_2 and $Ti_3C_2T_x$ composites, the adsorption energy of composites toward NH_3, acetone, ethanol, HCOH and CH_3COCH_3 molecular was calculated and the result was illustrated in Fig. S2. The adsorption energy of MoS_2 and $Ti_3C_2T_x$ heterojunction toward NH_3 is much more negative than that of acetone, ethanol, HCOH and CH_3COCH_3 molecular. In general, the more negative adsorption energy behaves the stronger adsorption ability. Hence, the composites of MoS_2 and $Ti_3C_2T_x$ behave the excellent selectivity to NH_3 molecular at RT. Fig. 5**g** shows the response of MoS_2/MXene-c at different humidity levels. The response rises with increase of humidity from 50 % to 70 %. After that value, the response becomes poor. With the increases in humidity, the NH_3 molecular would solvate into NH^{4+} ions on the surface of sensor and then react with adsorbed oxygen ions, leading to a higher sensing. While, when the humidity is to high, the partial active sites of sensing materials are occupied by the water molecules, leading to the lower sensing response [28]. Fig. 5**h** shows the response of $MoS_2/Ti_3C_2T_x$-c composite to 100 ppm NH_3 in three consecutive cycles. The response decreases obviously after three cycles. The long-term stability of $MoS_2/Ti_3C_2T_x$-c is evaluated by recording the baseline resistance and room-temperature response for 15 days. In Fig. 5i, the obvious change in baseline resistance was observed. The relative standard deviation (RSD) of resistance and response was about 12.42 % and 18.64 %, respectively. Additionally, the response after 15 days was decreased by only 27.93 %, indicating that the desired excellent long-term stability may not yet be reached.

Fig. 6 shows the resistance change curves of MoS_2 and $MoS_2/Ti_3C_2T_x$ composites toward 300 ppm NH_3 at RT. Upon exposure to NH_3, the resistance of MoS_2 decreases, showing an n-type semiconducting behavior. For the MoS_2 and $Ti_3C_2T_x$ composites, if the concentration of thiourea during preparation is added up from 0.7 *wt*% to 1.15 *wt*%, the resistance of composites increases, showing the p-type semiconducting behavior. Upon further increase, the resistance decreases, showing the n-type semiconducting behavior. At low thiourea concentrations during preparation, the MoS_2 in composites contains a large number of S vacancies, resulting in the fermi level moves down to the valence band and behaving the P-type semiconducting behavior [29–32]. When the sensor is exposed to NH_3, the S vacancies on the surface of MoS_2 can act as the active sites for adsorption of NH_3. NH_3 molecules are absorbed, and holes are combined with the electrons released from NH_3 molecular to enhance the resistance. At high thiourea concentrations, some of S is used for synthesis of MoS_2, and the rest provides free electrons, resulting in the electron is the main carriers in the composites. If NH_3 adsorbs on the surface of composites, electrons are captured and then released into the conduction band of MoS_2 to increase the conductivity [33,34]. Fig. S3 shows the response and recovery time of composites prepared with different thiourea concentration, and reveals that $MoS_2/Ti_3C_2T_x$ composites exhibit the long response and recovery time. At RT, the average free path and velocity of NH_3 molecules are relatively low and thus the diffusion rate of NH_3 molecular is slow at RT. There is need long time for NH_3 molecules diffusing to the active surface sites of sensor or desorption from the surface of sensor, resulting in the long response and recovery time. In addition, the carrier mobility of MoS_2 and $Ti_3C_2T_x$ composites at RT is low. The charge transfer efficiency between the sensor and NH_3 molecular in the adsorption and desorption process is slow, resulting in slower response and recovery rate. In addition, the comparison of NH_3-sensing performance of $MoS_2/Ti_3C_2T_x$ composites in this work with other previous work is presented in Table S1 [29,35–43]. The pure $Ti_3C_2T_x$ show the lower NH_3-sensing response, longer response and recovery time at RT [35–37]. The MoS_2, WO_3 and ln_2O_3/rGO composites show the excellent NH_3-sensing response. While, the optimal working temperature is very high, limiting its application [29,38,39]. For the $Ti_3C_2T_x$/graphite, $Ti_3C_2T_x$/TiC and MoS_2/Ti_3C_2 composites, the response is still lower than that of $MoS_2/Ti_3C_2T_x$ composites [40–42]. Hence, fabrication of $MoS_2/Ti_3C_2T_x$ composites in this work could achieve excellent room-temperature NH_3-sensing performance.

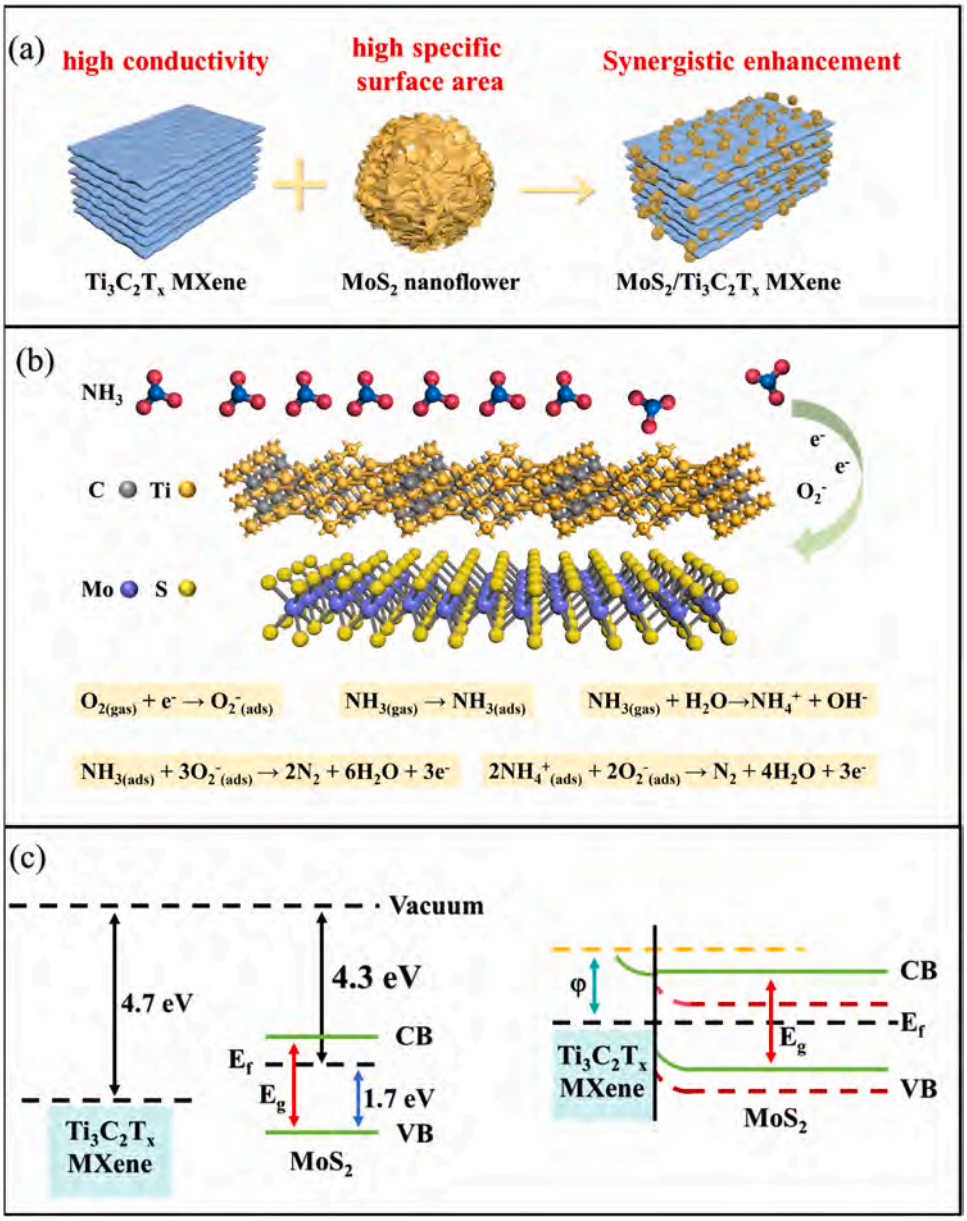

Fig. 7. Schematic illustration of (a) $MoS_2/Ti_3C_2T_x$ composite, (b) NO_2 adsorbed by the composite and (c) energy band structure diagram of $MoS_2/Ti_3C_2T_x$ composite.

3.3. *Gas-sensing mechanism*

The enhanced NH_3 sensing property of composite is ascribed to the abundant adsorption sites of MoS_2 flakes, high conductivity of $Ti_3C_2T_x$, and heterojunction enhancement. As displayed in Fig. 7a, the layer structure of $Ti_3C_2T_x$ has the large specific surface area and high conductivity. Owing to Van der Waals' force, $Ti_3C_2T_x$ tends to agglomerate easily, thus limiting the NH_3 response at RT. After combining with MoS_2, because of interfacial interaction, the agglomeration of $Ti_3C_2T_x$ is mitigated, giving rise to more active sites for adsorption of NH_3 molecules and behaving the better NH_3-sensing properties. Fig. 7**b** shows the schematic diagram of NH_3 adsorption process. In air, the O_2 molecular are adsorbed on the surface of MoS_2 and thus the chemical adsorbed oxygen ions (O_2^-) are formed [44]. In NH_3, the adsorbed NH_3 molecular would react with O_2^- ions, releasing the electrons back to the surface of MoS_2. At same time, the metallic $Ti_3C_2T_x$ would facilitate electron transport in MoS_2 and $Ti_3C_2T_x$ heterostructure. In addition, besides O_2^- ions, the H_2O molecular in air is also adsorbed on the surface of MoS_2 during NH_3-sensing response and the NH_3 molecular would solvate into NH^{4+} ions and then react with adsorbed O_2^- ions, leading to a higher sensing response [45,46]. While, at higher humidity, the water molecular would inhibit the electron exchange between NH_3 molecular and sensing materials, resulting in poor NH_3-sesning response. In Fig. 7**c**, the work function of $Ti_3C_2T_x$ MXene is higher than that of MoS_2. When MoS_2 is contacted with $Ti_3C_2T_x$ MXene, the electrons are transferred from MoS_2 to MXene until the Fermi level reaches a balance. The Schottky barrier (SB) junction is formed at interface. Upon exposure to NH_3, the Fermi level of MoS_2 rises far from the valence band, causing the decrease of space charge region, promoting the electron transfer at interface and the depletion region increases after the adsorbed gas molecules release electrons. Therefore, the response of gas sensor is enhanced. Additionally, to reveal the role of adsorbed oxygen, the response of $MoS_2/-Ti_3C_2T_x$-c to NH_3 in N_2 and O_2 are conducted. In Fig. 8, the response to NH_3 in O_2 is higher than that in N_2. That confirms the adsorbed chemical oxygen plays the important role on the NH_3-sensing response.

Furthermore, to reveal the heterojunction enhancement mechanism, the density of states (DOS) and partial density of states (PDOS) of MoS_2, $Ti_3C_2T_x$ and $MoS_2/Ti_3C_2T_x$ heterojunction are calculated by the first-

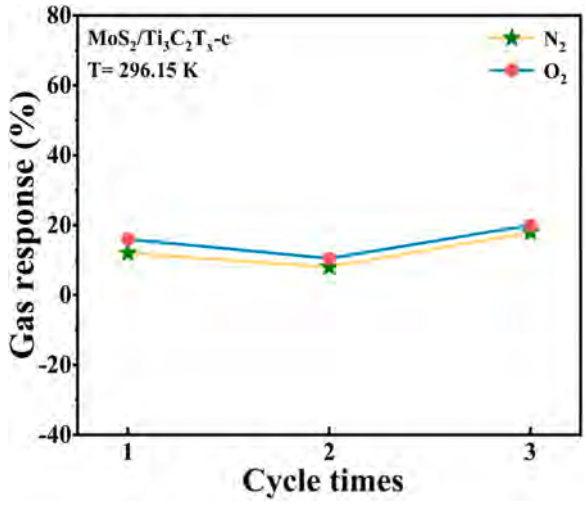

Fig. 8. The response of $MoS_2/Ti_3C_2T_x$-c sensor to NH_3 at different backing gases.

principles calculation. In Fig. 9a and b, the conduction band bottom (CBB) and valence band top (VBT) of MoS_2 are mainly composed of Mo *d* and S *p* states, respectively. The bandgap is about 1.9 eV. Whereas the CBB and VBT of $Ti_3C_2T_x$ MXene are mainly composed of Ti 3*d* and C *2p* states, respectively. The CBB and VBT are overlapped at fermi level, behaving metal property (Fig. 9c and d). For the MoS_2 and $Ti_3C_2T_x$ heterojunction, the CBB is mainly dominated by the Ti *d* state, while the VBT is mainly contributed by the Mo *d* and S *p* states (Fig. 9e and f). The bandgap is also nearly zero, the electron is transferred easily from VBT to CBB. Therefore, fabrication of MoS_2 and $Ti_3C_2T_x$ heterojunction could promote the charge transfer and enhance gas sensing properties of composite.

4. Conclusion

In summary, the flower-like MoS_2 was grown on the surface of $Ti_3C_2T_x$ by the hydrothermal method and applied for detection of NH_3 at RT. Compared with pure $Ti_3C_2T_x$ and MoS_2, the response of composites for 300 ppm NH_3 was increased by 5.53 and 30.6 times, respectively. Furthermore, it's surprisingly found that the semiconducting behavior of prepared MoS_2 and $Ti_3C_2T_x$ composites are highly dependent on the concentration of thiourea during preparation. At low thiourea concentration, the composites exhibit the p-type semiconducting behavior, but n-type properties if the thiourea concentration is higher. According to the DFT calculations, the conduction band and valence band of $MoS_2/Ti_3C_2T_x$ heterojunction is overlapped at Fermi level, showing metallicity properties. The electron is transferred easily from VBT to CBB, promoting the activity of charge transfer and enhance gas sensing properties of composite. These findings collectively suggest that the MoS_2 and $Ti_3C_2T_x$ composites could be used as a promising sensing material for NH_3 detection.

CRediT authorship contribution statement

Paul K Chu: Writing – review & editing, Validation, Writing – original draft. **Ai TaoTao:** Funding acquisition, Investigation, Formal analysis. **Xinyu Lei:** Funding acquisition, Data curation, Formal analysis. **Zhang Lizhai:** Writing – original draft, Funding acquisition, Writing – review & editing, Investigation. **Dingyuan Wang:** Formal analysis, Conceptualization, Data curation. **Henghui Sun:** Resources, Software, Data curation. **Fei Ma:** Investigation, Data curation, Formal analysis. **Baisong Chen:** Project administration, Resources, Methodology.

Declaration of Competing Interest

The authors declare that they have no known competing financial interests or personal relationships that could have appeared to influence the work reported in this paper.

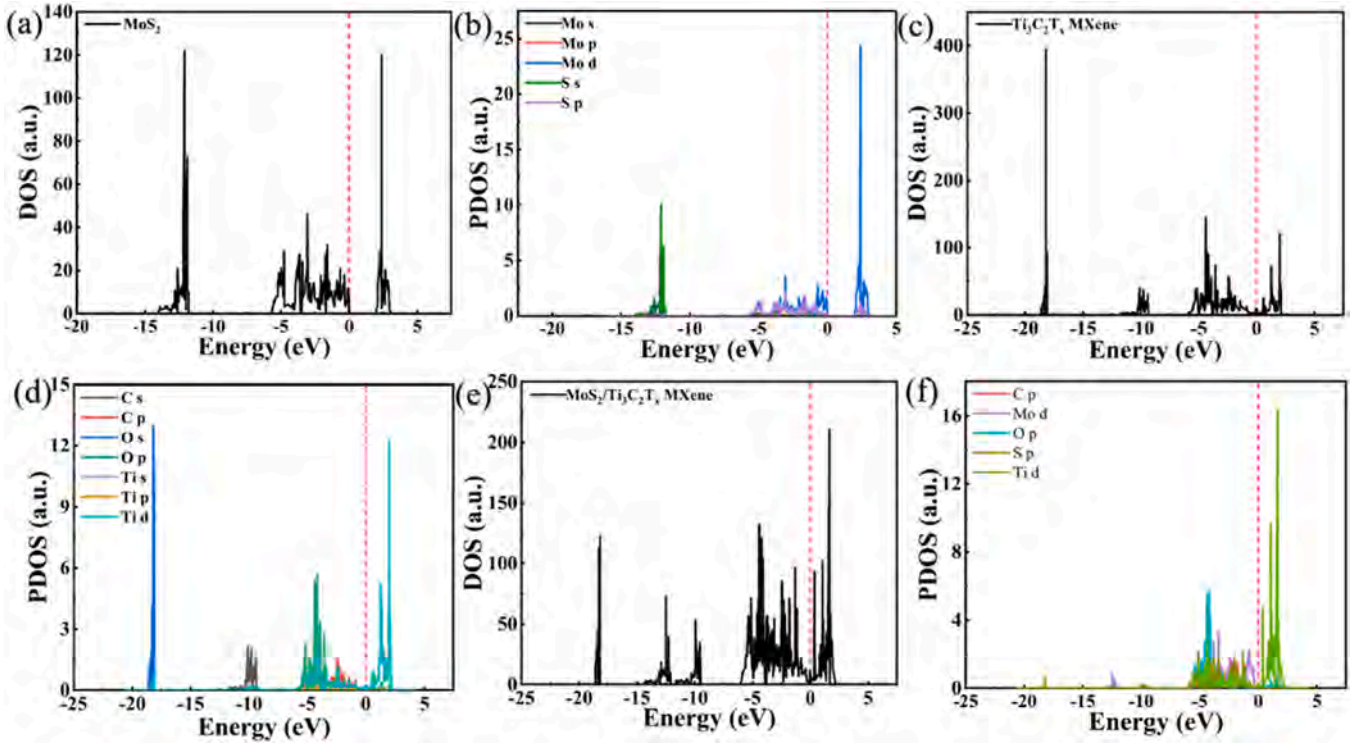

Fig. 9. The DOS and PDOS of (a, b) MoS_2, (c, d) $Ti_3C_2T_x$, and (e, f) MoS_2/MXene heterojunction.

Acknowledgments

This work was jointly supported by the Natural Science Foundation of Shaanxi Province (2023-JC-QN-0476), Shaanxi University of Technology Research Grant (no. SLGRCQD2207), Scientific research project of Shaanxi Provincial Education Department (no.23JK0375), Science and technology program for overseas students of Shaanxi province (2023016) and City University of Hong Kong Donation Research Grants (DON-RMG nos. 9229021 and 9220061).

Supporting Information

Comparison of sample material performance with reference, Sample response and recovery times.

Appendix A. Supporting information

Supplementary data associated with this article can be found in the online version at doi:10.1016/j.jallcom.2025.182542.

References

[1] S.B. Ambade, R.B. Ambade, W. Eom, S.H. Noh, S.H. Kim, T.H. Han, 2D Ti_3C_2 MXene/WO_3 Hybrid Architectures for high-rate supercapacitors, Adv. Mater. Interfaces 5 (2018) 1801361.
[2] Y. Zhou, C. Gao, Y.C. Guo, UV-assisted ultrasensitive trace NO_2 Gas sensing based on few-layer MoS_2 nanosheet–ZnO Nanosheet–ZnO nanowire heterojunctions at Room Temperature, J. Mater. Chem. A. 6 (2018) 10286–10296.
[3] H. Liu, H. Yu, J. Wang, F. Xia, C. Wang, J. Xiao, $LaNbO_4$ as an electrode material for mixed-potential CO gas sensors, Sens. Actuators B Chem. 352 (2022) 130981.
[4] K. Ko, J. Lee, H. Chung, Highly efficient colorimetric CO_2 sensors for monitoring CO_2 leakage from carbon capture and storage sites, Sci. Total Environ. 729 (2020) 138786.
[5] P. Li, B. Wang, C. Qin, C. Han, Y. Wang, Band-gap-tunable CeO_2 nanoparticles for room-temperature NH_3 gas sensors, Ceram. Int. 46 (2020) 19232–19240.
[6] P.M. Mannucci, M. Franchini, Health effects of ambient air pollution in developed countries, Int. J. Environ. Res. Public Health 14 (2017) 1048.
[7] B. Yang, X. Li, W. Yuan, Z. Li, N. Lu, S. Wang, Y. Wu, S. Fan, Z. Hua, Efficient NH_3 detection based on MOS sensors coupled with catalytic conversion, ACS Sens 5 (2020) 1838–1848.
[8] D. Kuang, X. Guo, Z. Zhu, Y. Ding, Y. He, Enhanced room temperature ammonia response of 2D-$Ti_3C_2T_x$ MXene decorated with $Ni(OH)_2$ nanoparticles, Ceram. Int. 47 (2021) 19471–19480.
[9] L.Z. Zhang, J.Y. Xu, D.Y. Wang, X.Y. Lei, H.H. Sun, Y.H. Huang, F. Ma, T.T. Ai, P. K. Chu, Enhanced room-temperature NH_3-sensing performance of $Ti_3C_2T_x$ MXene decorated with CeO_2 nanoparticles, ACS Appl. Nano Mater. 8 (2025) 12090–12099.
[10] Y. Tan, J. Xu, Q. Li, W. Zhang, C. Lu, X. Song, L. Liu, Y. Chen, Sensitivity-enhanced, room-temperature detection of NH_3 with alkalized $Ti_3C_2T_x$ MXene, Nanomaterials 14 (2024) 680.
[11] P. Khakbaz, M. Moshayedi, S. Hajian, M. Soleimani, B.B. Narakathu, B.J. Bazuin, P. Mahdi, M.Z. Atashbar, Titanium carbide MXene as NH_3 sensor: realistic first-principles study, J. Phys. Chem. C. 123 (2019) 29794–29803.
[12] M. Wu, M. He, Q. Hu, Q. Wu, G. Sun, L. Xie, Z. Zhang, Z. Zhu, A. Zhou, Ti_3C_2 MXene-based sensors with high selectivity for NH_3 detection at room temperature, ACS Sens 4 (2019) 2763–2770.
[13] X. Guo, Y. Ding, D. Kuang, Z. Wu, X. Sun, B. Du, C. Liang, Y. Wu, W. Qu, L. Xiong, Y. He, Enhanced ammonia sensing performance based on MXene-$Ti_3C_2T_x$ multilayer nanoflakes functionalized by tungsten trioxide nanoparticles, J. Colloid Interface Sci. 595 (2021) 6–14.
[14] M. Zhou, Y. Han, Y. Yao, L. Xie, X. Zhao, J. Wang, Z. Zhu, Fabrication of $Ti_3C_2T_x$/In_2O_3 nanocomposites for enhanced ammonia sensing at room temperature, Ceram. Int. 48 (2022) 6600–6607.
[15] S.H. Lee, W. Eom, H. Shin, R.B. Ambade, J.H. Bang, H.W. Kim, T.H. Han, Room-temperature, highly durable $Ti_3C_2T_x$ MXene/graphene hybrid fibers for NH_3 gas sensing, ACS Appl. Mater. Interfaces 12 (2020) 10434–10442.
[16] G. Kresse, J. Furthmüller, Efficient iterative schemes for ab initio total-energy calculations using a plane-wave basis set, Phys. Rev. B 54 (1996) 11169.
[17] G. Kresse, J. Furthmüller, Efficiency of Ab initio total energy calculations for metals and semiconductors using a plane-wave basis set, Comput. Mater. Sci. 6 (1996) 15–50.
[18] J.P. Perdew, K. Burke, M. Ernzerhof, Generalized gradient approximation made simple, Phys. Rev. Lett. 77 (1996) 3865–3868.
[19] C. You, T. Fu, C. Li, X. Song, B. Tang, X. Song, Y. Yang, Z. Deng, Y. Wang, F. Song, A Latent-fire-detecting olfactory system enabled by ultra-fast and sub-ppm ammonia-responsive $Ti_3C_2T_x$ MXene/MoS_2 sensors, Adv. Funct. Mater. 32 (2022) 2208131.
[20] S. Kim, H. Shin, J. Lee, C. Park, Y. Ahn, H.J. Cho, S. Yuk, J. Kim, D. Lee, I.D. Kim, Three-dimensional MoS_2/MXene heterostructure aerogel for chemical gas sensors with superior sensitivity and stability, ACS Nano 17 (2023) 19387–19397.
[21] H. Long, A. Harley-Trochimczyk, T. Pham, Z. Tang, T. Shi, A. Zettl, C. Carraro, M. A. Worsley, R. Maboudian, High surface area MoS_2/graphene hybrid aerogel for ultrasensitive NO_2 detection, Adv. Funct. Mater. 26 (2016) 5158–5165.
[22] L.T. Duy, D.J. Kim, T.Q. Trung, V.Q. Dang, B.Y. Kim, H.K. Moon, N.E. Lee, High performance three-dimensional chemical sensor platform using reduced graphene oxide formed on high aspect-ratio micro-pillars, Adv. Funct. Mater. 25 (2015) 883–890.
[23] J.A. Robinson, E.S. Snow, Ş.C. Bădescu, L.R. Thomas, T.L. Reinecke, F.K. Perkins, Role of defects in single-walled carbon nanotube chemical sensors, Nano Lett. 6 (2006) 1747–1751.
[24] T.K. Nguyen, S. Jeong, J.S. Youn, S. Ahn, K.H. Nam, C.M. Paek, K.J. Jeon, Insight into mechanism of temperature-dependent limit of NO_2 detection using monolayer MoS_2, Sens. Actuators B Chem. 329 (2020) 129138.
[25] J.B. Liu, J.Y. Hu, C. Liu, Y.M. Tian, X. Peng, Y. Zhang, Mechanically exfoliated MoS_2 nanosheets decorated with SnS_2 nanoparticles for high-stability gas sensors at room temperature, Rare Met 40 (2021) 1536–1544.
[26] V.T. Le, Y. Vasseghian, V.D. Doan, T.T.T. Nguyen, T.T.T. Vo, H.H. Do, K.B. Vu, V. A. Tran, Flexible and high-sensitivity sensor based on Ti_3C_2–MoS_2 MXene composite for the detection of toxic gases, Chemosphere 291 (2022) 133025.
[27] R. Tian, Y. Ding, Q. Wang, P. Song, Designing advanced 2D/2D heterojunctions of MoS_2 nanosheets/$Ti_3C_2T_x$ MXene in gas-sensing applications, Vacuum 222 (2024) 112991.
[28] F. Rigoni, S. Freddi, S. Pagliara, Humidity-enhanced sub-ppm sensitivity to ammonia of covalently functionalized single-wall carbon nanotube bundle layers, Nanotechnology 28 (2017) 255502.
[29] P.H. Wen, H.Y. Zheng, T.J. Hsueh, A WO_3-NPs/MEMS NH_3 gas sensor, J. Electrochem. Soc. 170 (2023) 037506.
[30] Y. Chen, H. Fu, Y. Bai, X. Yang, S. Xiong, D. Han, X. An, Room-temperature NH_3-sensor: SnO_2@PANI core-shell hollow spheres, Sens. Actuators B Chem. 412 (2024) 135784.
[31] Z. Wang, X. Chang, J. Li, X. Zhu, Y. Zhang, D. Wang, Y. Jiang, S. Sun, Room-temperature NH_3 sensor based on $CoFe_2O_4$/PANI composite with porous structure, Mater. Res. Bull. 175 (2024) 112774.
[32] C. Zhang, L. Yu, S. Li, L. Cao, X. He, Y. Zhang, C. Shi, K. Liu, X. Fan, High conductivity of 2D hydrogen substituted graphene nanosheets for fast recovery NH_3 gas sensors at room temperature, Carbon 225 (2024) 119090.
[33] X. Zhu, J. Li, X. Chang, W. Gao, X. Chen, S. Niu, S. Sun, Room temperature gas sensors for NH_3 detection based on SnO_2 films and lamellar-structured $Ti_3C_2T_x$ MXene heterojunction nanocomposites, Appl. Surf. Sci. 660 (2024) 159976.
[34] D.J. Dmonte, A. Bhardwaj, P. Kavraz, R. Slobodian, J. Antos, O. Sisman, D. Galusek, T. Fisher, S. Mathur, I. Kuritka, Detection of NH_3 gas using $CrVO_4$ nanoparticles, Sens. Actuators B Chem. 406 (2024) 135380.
[35] M. Wu, M. He, Q.K. Hu, Q.H. Wu, G. Sun, L.L. Xie, Z.Y. Zhang, Z.G. Zhu, A.G. Zhou, Ti_3C_2 MXene-based sensors with high selectivity for NH_3 detection at room temperature, ACS Sens 4 (2019) 2763–2770.
[36] S.J. Kim, H.J. Koh, C.E. Ren, O. Kwon, K. Maleski, S.Y. Cho, B. Anasori, C.K. Kim, Y. K. Choi, J. Kim, Y. Gogotsi, H.T. Jung, Metallic $Ti_3C_2T_x$ MXene gas sensors with ultrahigh signal-to-noise ratio, ACS Nano 12 (2018) 986–993.
[37] Q. Zhao, Y.L. Li, Z.X.L. Zhang, L. Dai, X.H. Liu, Y.H. Sun, D. Zhao, N. Zhu, A flexible ammonia sensor based on MXene membrane with high sensitivity, Electroanalysis 36 (2024) e202400019.
[38] Y. Xiong, W.D. Liu, K.C. Wu, T. Liu, Y.M. Chen, X.Z. Wang, J. Tian, Constructing ultrathin defective Co_3O_4/MoS_2 nanosheets based 2D/2D heterojunction toward room temperature NH_3 detection, J. Alloy. Compd. 927 (2022) 166962.
[39] P.K. Mishra, G. Murali, T.H. Kim, J.H. Kim, Y.J. Lim, B.S. Kim, P.P. Sahay, S.H. Lee, Nanocube In_2O_3@ RGO heterostructure based gas sensor for acetone and formaldehyde detection, RSC Adv. 7 (2017) 38714–38724.
[40] C.E. Shuck, M.K. Han, K. Maleski, K. Hantanasirisakul, S.J. Kim, J.H. Choi, W.E. B. Reil, Y. Gogotsi, Effect of Ti_3AlC_2 MAX phase on structure and properties of resultant $Ti_3C_2T_x$ MXene, ACS Appl. Nano Mater. 2 (2019) 3368–3376.
[41] S. Atkare, S.D. Kaushik, S. Jagtap, C.S. Rout, Room-temperature chemiresistive ammonia sensors based on 2D MXenes and their hybrids: recent developments and future prospects, Dalton Trans. 52 (2023) 13831–13851.
[42] Z.Z. Guo, H.R. Zhang, J.M. Zhang, N. Alwadie, L.Y. Duan, Y.L. Li, Z.Y. Hou, V. D. Dao, M. S. I, Tailoring MoS_2 nanoflakes over MXenes nanobelts for efficient ammonia detection at room temperature, J. Alloy. Compd. 1010 (2025) 177710.
[43] L.C.T. Cao, M.H. Zhou, P. Opaprakasit, P. Sreearunothai, Y.K. Nagao, S. Boonruang, H. Fallah, S.F. Tseng, S.H. Hsu, Facile fabrication of oxygen-enriched MXene-based sensor and their ammonia gas-sensing enhancement, Adv. Mater. Interfaces 10 (2023) 2300166.
[44] Y. Li, H. Li, B. Dong, X. Liu, G. Feng, L. Zhao, Improved NH_3 gas sensing performance of femtosecond-laser textured silicon by the decoration of Au nanoparticles, Phys. Status SolidiR. 18 (2024) 2400015.
[45] Y. Qin, X. Liu, J.H. Xie, Humidity-enhanced NH_3 sensor based on carbon quantum dots-modified SnS, Appl. Surf. Sci. 634 (2023) 157612.
[46] B.A.J. Lechner, Y. Kim, P.J. Feibelman, Solvation and reaction of ammonia in molecularly thin water films, J. Phys. Chem. C 119 (2015) 23052–23058.

Enhanced NH_3 sensing Performance of $Ti_3C_2T_x$ MXene Decorated with Flowered MoS_2

Lizhai Zhang[a,b,c], Xinyu Lei[a], Henghui Sun[a], Dingyuan Wang[a], Baisong Chen[d], Fei Ma[b], Taotao Ai[a]*, Paul K Chu[c*]*

[a] School of Materials Science and Engineering, Shaanxi University of Technology, Hanzhong 723001, Shaanxi, China

[b] State Key Laboratory for Mechanical Behavior of Materials, Xi'an Jiaotong University, Xi'an 710049, Shaanxi, China

[c] Department of Physics, Department of Materials Science and Engineering, and Department of Biomedical Engineering, City University of Hong Kong, Tat Chee Avenue, Kowloon, Hong Kong, China

[d] Faculty of Optoelectronic Engineering, Xidian University, Xi'an 710126, Shaanxi, China

* Address correspondence to: zhanglizhai0512@snut.edu.cn (L. Z. Zhang); aitaotao0116@126.com (T. T. Ai); paul.chu@cityu.edu.hk (P. K. Chu)

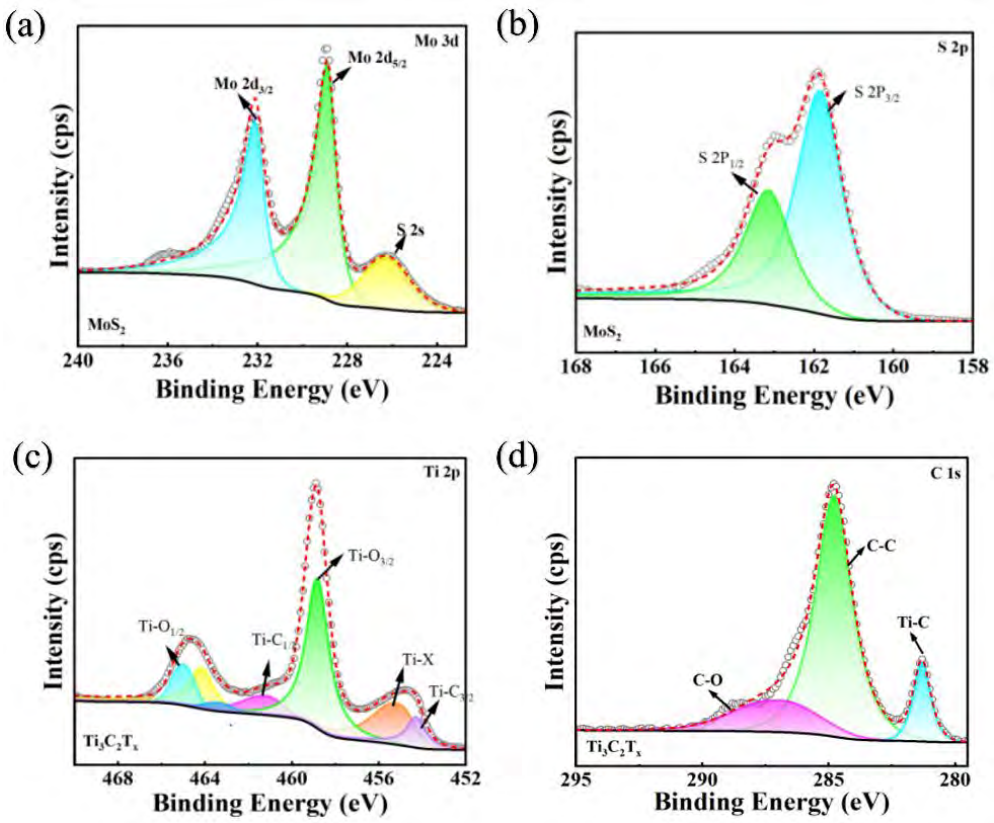

Fig. S1. The XPS spectra of MoS_2: (a) Mo 3d, (b) S 2p and $Ti_3C_2T_x$: (c) Ti 2p, (d) C1s.

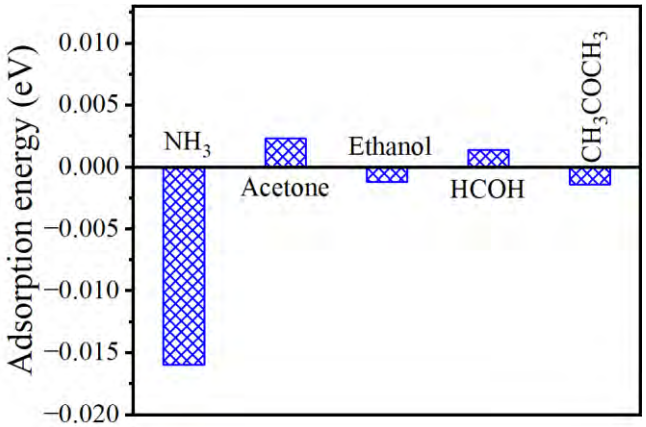

Fig. S2. The adsorption energy of MoS_2 and $Ti_3C_2T_x$ heterojunction toward NH_3, acetone, ethanol, HCOH and CH_3COCH_3 molecular.

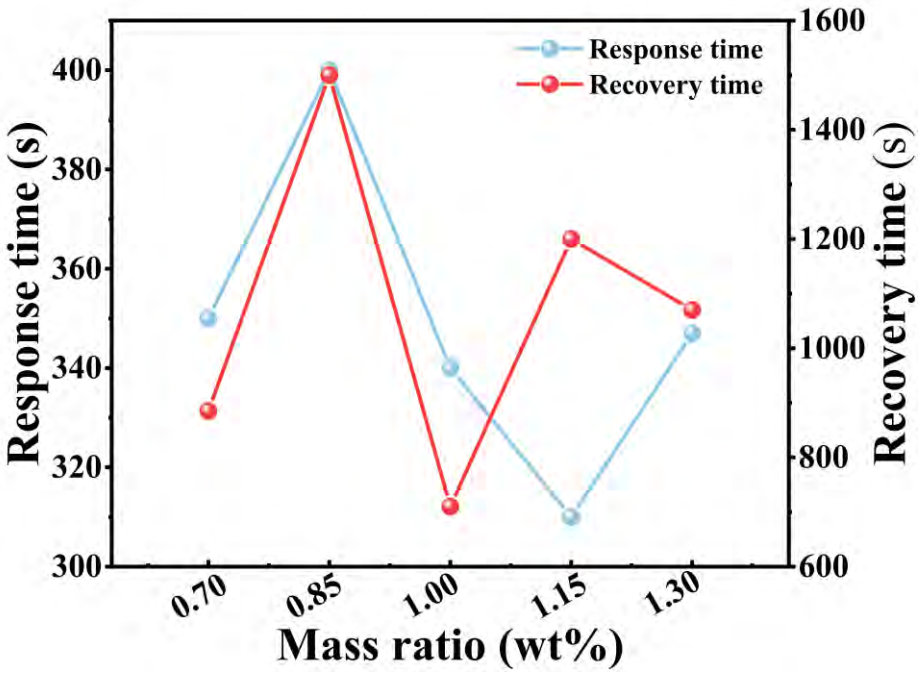

Fig. S3 Sample response and recovery times for different thiourea

Table S1. Comparison of NH_3-sensing performance of $MoS_2/Ti_3C_2T_x$ composites in this work with those in the previous work.

Sensing materials	concentration (ppm)	Response/recovery time (s)	Temperature (℃)	Response (%)	Ref.
$Ti_3C_2T_x$	500	120/230	RT	6.13	[35]
$Ti_3C_2T_x$	100	300/900	RT	0.8	[36]
$Ti_3C_2T_x$ membrane	0.5	41/100	RT	66.67	[37]
MoS_2	50	210/285	100	66.67	[38]
WO_3	1.3	59/47	142	16	[29]
In_2O_3/rGO	25	186/162	225	10.1	[39]
$Ti_3C_2T_x$/graphite	5	580/720	RT	0.55	[40,41]
$Ti_3C_2T_x$/TiC	5	568/860	RT	0.62	[40,41]
MoS_2/Ti_3C_2	100	40/20	RT	10	[42]
$Ti_3C_2T_x$/PANI	20	143/293	RT	48.25	[43]
$MoS_2/Ti_3C_2T_x$ composites	300	258/780	RT	30.7	In this work